# Modulation mechanisms of Marine Atmospheric Boundary Layer

# at the Brazil-Malvinas Confluence region

Ricardo de Camargo[1]

Enzo Todesco[1]

Luciano Ponzi Pezzi[2]

Ronald Buss de Souza[3]

[1]Department of Atmospheric Sciences, Institute of Astronomy, Geophysics and Atmospheric Sciences, University of Sao Paulo

[2]Earth Observation General Coordination, National Institute for Space Research

[3]South Regional Center for Space Research, National Institute for Space Research

**Abstract**

The influence of the Brazil-Malvinas Confluence (BMC) region on the marine atmospheric boundary layer (MABL) is investigated through *in situ* data analysis of five different cruises (2004 to 2008) and numerical experiments with a regional atmospheric model. Two different groups of numerical experiments were performed in order to evaluate the relevance of static stability and hydrostatic balance physical mechanisms for the MABL instability. The first group used monthly climatological SST as bottom boundary condition while the second used daily updated AMSR-E SST data together with radiosondes and surface data assimilation. A reasonable agreement between numerical results and QuikScat wind data was observed through correlation coefficients and mean square error values. In terms of the horizontal structure of the MABL, stronger winds were found over the warm side of the BMC region as well as over the thermal front itself, which supports the co-existence of both modulation mechanisms. The analyzed patterns of surface atmospheric thermal advection showed a clear interaction between the synoptic and regional scales. The signature of the oceanic thermal front (almost meridionally oriented) on the air temperature at 2 m makes the temperature advection strongly determined by the zonal component of the wind. The analysis of momentum budget terms did not show a clear and reasonable explanation of the existence or predominance of the modulation mechanisms, and it also suggested the relevance of other effects, such as the idea based on unbalanced Coriolis force and turbulence/friction effects.

## 1. Introduction

Strong thermal fronts at the sea surface temperature (SST) distribution are features that can occur seasonally in the tropics during Tropical Instability Waves (TIW) events [*Legeckis,* 1977] and there are many studies on atmospheric boundary layer modulation during these events, exploring air-sea interactions due to large-scale and mesoscale circulation patterns of the ocean [*Lindzen and Nigam,* 1987; *Wallace et al.,* 1989; *Pezzi et al.,* 2004; *Seo et al.,* 2007a, 2007b]. Comprehensive reviews on air-sea interaction over oceanic thermal fronts covering spatial-temporal scales from mesoscale to large-scale can be found in *Small et al.* [2008] and *Chelton and Xie* [2010], and references therein.

At higher latitudes, in the confluence regions between basin scale gyres, thermal contrasts occur during the entire year, and some evidence of such mechanisms of atmospheric modulation have recently been studied, e.g. *Pezzi et al.* [2005, 2009] and *Acevedo et al.* [2010]. One of the most important of these thermal front regions is located in the South-western Atlantic, at the Brazil-Malvinas Confluence region [*Reid et al.,* 1977; *Legeckis* 1977; *Olson et al.,* 1988; *Podestá,* 1997; *Souza and Robinson,* 2004; *Lentini et al.,* 2001, 2006], hereafter BMC. This thermal contrast is very clear from space and has a seasonal meridional displacement driven by the wind curl, as well as by the intensity of the Brazil and Malvinas currents.

The response of the marine atmospheric boundary layer (MABL) to the spatial distribution of SST in the tropics has been studied by *Lindzen and Nigam* [1987], who suggested that variations in the SST directly influence the variations of the temperature of the air right above, and consequently on the surface pressure, through hydrostatic balance: lower (higher) surface pressure is located over relatively warmer (colder) water. In this mechanism, the surface wind moves toward the lower pressure values, e.g., toward higher SST values.

Another important consideration was presented by *Wallace et al.* [1989], when they analyzed measurements over the Eastern Tropical Pacific. They proposed that SST directly influences the density stratification at the MABL, through vertical stability change. According to this behavior, both buoyancy and turbulence rise over relatively warm waters yielding to stronger surface winds. The opposite situation is found over relatively colder waters.

Numerical studies in the Tropical Pacific Ocean conducted by *Small et al.* [2005] showed some evidence of the atmospheric surface pressure forcing. They suggested that surface pressure anomalies are not accompanied by SST anomalies in the particular case of TIW. Their results showed that the mechanism presented by *Wallace et al.* [1989] could not be relevant due to the advection of temperature and humidity by the mean wind. They also showed that the pressure effect is enough to cause induced winds in phase with SST.

*Tokinaga et al.* [2005] described for the first time the SST effects over the surface wind fields and vertical stability of the MABL in the BMC region, providing a detailed analysis of climatological patterns of air-sea interaction and showing that over this region positive correlation is found between SST and surface wind magnitude. *Pezzi et al.* [2005], using high resolution *in situ* data, suggest that in the absence of large-scale atmospheric systems, the oceanic front that characterized the BMC region will modulate the MABL. Both studies corroborate the *Wallace et al.* [1989] hypothesis.

*Spall* (2007) presented an interesting idealized numerical study with a fully coupled atmospheric-ocean model showing that, in mid-latitudes and strong wind regimes, the coupling mainly occurs due to the change in turbulent mixing conditions and the corresponding unbalanced Coriolis force near the thermal front. For lower latitudes and weaker winds, however, static stability and hydrostatic balance dominate.

*Acevedo et al.* [2010] performed a climatological study of the synoptic cycle in the BMC region and presented 5 stages of classification: day -2, two days before the cold front system passage; day -1, one day before; day 0, low pressure over BMC region; day +1, one day after; day +2, two days after the frontal system passage. The different phases can induce distinct patterns of thermal advection in the BMC region, yielding different adjustment processes of the MABL.

The main aim of this study is to make a reasonable physical characteristics description and provide explanations for the different MABL stability behaviors seen over the warm and cold sides of the oceanic front. In order to do this, the physical processes that result in MABL modulation in the BMC region are investigated and described. Our results have shown that both static stability and hydrostatic balance, simultaneously or not, are the mechanisms responsible for the MABL instability. This study is conducted through *in situ* data analysis, atmospheric numerical experiments using observed data assimilation, and the analysis of components of the linear *momentum* equation. The numerical experiments were performed using the mesoscale regional model Brazilian developments in the Regional Atmospheric Modeling System (BRAMS)[1]. The *in situ* data of both ocean and atmosphere were collected during a sequence of austral spring cruises onboard the Brazilian Navy Oceanographic Support Ship (OSS) *Ary Rongel*, while crossing the BMC region. This activity is part of the program for measuring and analyzing the air-sea interactions specifically called Air-Sea Interaction at the Brazil-Malvinas Confluence (INTERCONF, Pezzi *et al.*, 2009) under the umbrella of Brazilian Antarctic *Program* (PROANTAR). The data set used is related to experiments made in November 2004 (called as OP23), October 2005 (OP24), October 2006 (OP25), October 2007 (OP26) and October 2008 (OP27).

---

[1] BRAMS information and source code can be found in http://brams.cptec.inpe.br/index.shtml.

The rest of the study is organized as follows. The observed data derived from satellite, in situ data measurements, numerical experiments and methodological analysis are described in the Section 2. The results, including the vertical and horizontal MABL stability analysis and both static stability and hydrostatic balance physical mechanisms for the MABL instability, are in Section 3. The final discussion and conclusions are given in Section 4.

## 2. Data and Methodology

### 2.1 Satellite Data and Atmospheric Analysis

Data obtained by Advanced Microwave Scanning Radiometer of Aqua satellite (AMSR-E) were used to identify the position of the thermal front in the BMC region to guide the location of the observations during the cruises, as well as to specify the SST values considered in the numerical simulations of this study. AMSR-E is a passive microwave sensor able to sample the ocean surface to estimate SST even in cloudy conditions, and, because of this, is being employed to describe SST fields in the BMC region where clouds are common [*Souza et al.,* 2006].

In addition, wind vectors from the Seawinds scatterometer of the QuikScat satellite are used to analyze and verify numerical experiments. The physical principle of the scatterometer is to measure the scattered reflection from the ocean surface of a radar pulse emitted by the sensor, where the capillary waves produced locally by the surface wind are primarily responsible for the observed scattering. This sensor can measure winds from 3 to 20 m/s, with an accuracy of 2 m/s in speed and 20 degrees in direction, with a spatial resolution of 25 km. Nevertheless, the acquisitions are affected by all phenomena that destroy capillary waves, such as rain and wind over 20 m/s [*Wentz et al.,* 2001; *Hoffmann & Leidner,* 2005]. The data sets from QuikScat

have already been used in the investigation of atmospheric manifestation of TIW at the Tropical Pacific [*Liu et al.,* 2000].

Large-scale conditions for the specific measured periods were obtained through the use of Global Forecast System (GFS) operational atmospheric analysis produced by the National Centers for Environment Prediction (NCEP). This atmospheric dataset is available for the entire globe, with time resolution of 6 hours, spatial resolution of 1 degree in latitude and longitude, and 17 vertical pressure levels. These data were used for the synoptic analyses and the specification of initial and boundary conditions for the mesoscale numerical experiments.

## 2.2 *In Situ* Data

The Brazilian Navy OSS *Ary Rongel*, as part of the activities of PROANTAR, departs from Brazil every year during October or November towards Antarctica to supply and maintain the Brazilian research station in the Antarctic and carry out routine summer activities. During the cruise, scientific projects collect atmospheric and oceanic data; one of these projects, the Air-Sea Interaction at the Brazil-Malvinas Confluence Region (hereafter referred to INTERCONF, based on its Portuguese acronym), started to make simultaneous observations of XBT and radiosondes over the oceanic thermal front during OP23, in October–November 2004.

In this study, we have considered data from five cruises, called in Brazil "Antartic Operation 23 (hereafter OP23) to 2008 (OP27) during over five consecutive years starting in 2004. All of them took place in the same period of the year. Besides the XBT and radiosondes data on the thermal front, data from the meteorological station of the ship are also part of the interest of the INTERCONF (Figure 1). The importance of this kind of observation is fully described in *Pezzi et al.* [2005], which

also includes the initial investigation on the air-sea interaction processes in the BMC region.

The BMC region was sampled in 3 sub-regions: (i) the warmer BMC side over BC; (ii) the thermal front (TF) itself that denotes the transition region between BC and MC, which is located over the largest SST gradient region; and (iii) the colder BMC side over MC. An explicit identification of the location as well as the date and time of each radiosonde vertical profile is presented in Table 1.

## 2.3 Numerical Experiments with BRAMS

The BRAMS atmospheric model is a cooperative project between Brazilian universities and research institutes, whose main aim is to produce a new version of the Regional Atmospheric Modeling System (RAMS) [*Pielke et al.,* 1992], properly adjusted for the tropics and which could be used by Brazilian regional centers for weather forecasting. The original RAMS code was developed at Colorado State University in the early 1990's, and brought together established codes for cloud microphysics and dynamical core as it is a versatile numerical model which can be used for both micro and the large-scale, and is most frequently applied to mesoscale simulations [*Cotton et al.,* 2003].

BRAMS is based on the complete set of equations that characterize the evolution of the atmospheric state, which consider Newton's laws and fluid thermodynamics, including parameterizations of physical mechanisms such as turbulent diffusion, solar and earth radiation, wet processes for cloud formation, soil layers, vegetation, and others. The model contains a multiple grid nesting scheme, which can simultaneously solve different resolution meshes in a two-way nesting procedure, where the coarse mesh affects the finer mesh and vice-versa.

In addition to the atmospheric module, BRAMS has an isentropic analyses scheme called ISentropic ANalysis package (ISAN), which allows data assimilation from global models as well as surface and upper air to be used as initial and boundary conditions. The Observational Data Assimilation used in BRAMS is an alternative method that can be seen as a generalization of the observational nudging scheme, resulting in an efficient and suitable scheme. This procedure eliminates the problem of the time lag between measurement and the specific instant of assimilation by the model, using a pre-defined maximum time interval, which is checked at every model time step. It is important to stress that this scheme performs space interpolation based on the Kriging method to obtain three-dimensional fields of the observed values, as well as their co-variances. The combination of values and co-variances will introduce information only at the model grid points that are near the observation location.

Surface *in situ* data (sea level pressure, temperature, dew-point temperature, wind speed and direction) as well as upper air observations (pressure, geopotential height, temperature, relative humidity, wind speed and direction) were assimilated in all different grids used by the model. For surface and radiosonde data assimilation, BRAMS uses an objective analyses method based on *Barns* [1964] methodology.

The mesoscale model BRAMS was employed in order to quantify atmospheric phenomena representing physical processes of air-sea interaction that modulates MABL in the BMC region. The numerical simulations were selected to cover the whole *in situ* data period of collection for each cruise, from OP23 to OP27, corresponding respectively to 2004 until 2008. The simulations were performed using two grids: the coarse one with a spatial resolution of 40 km, and the nested one, with 10 km spatial resolution, both centered over the route of the cruises when the ship crossed the thermal front.

Two different groups of numerical experiments were performed in order to evaluate the importance of the mentioned physical mechanisms driven by SST patterns for the MABL instability. The first group, called CLIM, used climatological SST as a lower boundary condition, while the second, called OBS, used daily and dated AMSR-E SST data together with radiosondes and surface data assimilation. All the results discussed in this study are related to the nested grid with 10km resolution, called GRD10.

## 2.4 Horizontal *momentum* balance

In order to identify the physical processes acting on the MABL adjustment that could explain different behavior of the wind speed between warm and cold BMC sides, the horizontal components of the linear momentum equations were analyzed. The general form of the equations considering the total flow as a sum of an average value and its fluctuation can be written as:

$$\frac{\partial \bar{u}}{\partial t} = -\left(\left[\bar{u}\frac{\partial \bar{u}}{\partial x} + \bar{v}\frac{\partial \bar{u}}{\partial y}\right] + \bar{w}\frac{\partial \bar{u}}{\partial z}\right) - \left(\frac{1}{\rho_0}\frac{\partial \bar{p}}{\partial x}\right) + (f\bar{v}) - \left(\frac{\partial \overline{(u'u')}}{\partial x} + \frac{\partial \overline{(u'v')}}{\partial y} + \frac{\partial \overline{(u'w')}}{\partial z} + \overline{Fr_x}\right) \text{ Equation 1}$$

$$\frac{\partial \bar{v}}{\partial t} = -\left(\left[\bar{u}\frac{\partial \bar{v}}{\partial x} + \bar{v}\frac{\partial \bar{v}}{\partial y}\right] + \bar{w}\frac{\partial \bar{v}}{\partial z}\right) - \left(\frac{1}{\rho_0}\frac{\partial \bar{p}}{\partial y}\right) - (f\bar{u}) - \left(\frac{\partial \overline{(v'u')}}{\partial x} + \frac{\partial \overline{(v'v')}}{\partial y} + \frac{\partial \overline{(v'w')}}{\partial z} + \overline{Fr_y}\right) \text{ Equation 2}$$

where Equation 1 is related to the zonal direction and Equation 2 to the meridional component. For both, the left side is the local acceleration term, while the first bracket on the right is the advection term (with the horizontal and vertical components), the second brackets contain the term related to the pressure gradient, the third has the Coriolis term, and the fourth the residual that includes turbulent and friction terms. The evaluation of the balance between these terms was used to infer the possible processes that could explain the main differences found at surface wind speed.

## 3. Results

### 3.1 Model skill

The capability of the model can be verified instantly through a specific profile observed during OP23, where both radiosonde observation and model results were directly compared. Considering GRD10 model results with full assimilation (OBS setup), a good adjustment of the vertical profile within the MABL was verified, which brought the modeled variable close to the measured value (Figure 2). The wind components were slightly underestimated, but the model correctly represents the vertical profile. On the other hand, mixing ratio and potential temperature showed better adjustment.

The 10 meters-high wind fields obtained from GRD10/OBS experiments were compared to the corresponding QuikScat observations. In order to accurately make these comparisons, the model generated wind fields were taken as 3-day averages centered on those days where atmospheric radiosonde data collection was made. These 3-day averages were adopted in order to avoid unobserved areas within the modeled domain imposed by the QuikScat coverage scheme. These days are 2 November 2004, 28 October 2005, 27 October 2006, 16 October 2007, and 15 October 2008. The quantification of these representations was performed through spatial correlation and mean square errors (Figure 3).

The lowest correlation coefficient (0.71) was found for OP24 (Figure 3b), which also presented the highest mean square error (1.57 m/s). This can be interpreted as a relatively poor representation by the model. The other campaigns presented correlation coefficients ranging from 0.87 to 0.93 and mean square errors between 0.93 and 1.38 m/s, which are better representations (Figures 3a, 3c, 3d, 3e).

Another striking feature seen in Figure 3 is that QuikScat observations present stronger winds occurring more often over the BC warmer waters than over MC cold waters. BRAMS could not always capture this behavior.

## 3.2 Thermal advection patterns

Wind modulation can be analyzed in terms of the dominant synoptic atmospheric large-scale condition, according to the approach used in *Acevedo et al.* [2010], who classified each of the cruises based on frontal activity and thermal advection over BMC region using NCEP atmospheric reanalysis fields [*Kalnay et al.* 1996]. The classification adopted by *Acevedo et al.* [2010] is reproduced in Table 2.

The thermal advection classification used in *Acevedo et al.* [2010] does not consider the local structure of the air temperature pattern influenced by the BMC. In their work, thermal advection was estimated from the wind turning with height through thermal wind equation, while the present analysis considered the GRD10/OBS model results as input for temperature advection calculations, thus showing a possible interaction between the scales, the synoptic (large-scale) and mesoscale (local factor).

These patterns are considered in our analysis, which does not mean that in a pre-frontal situation associated with northerly flow there is always only warm advection (Figure 4). This is what happens in OP23, OP25 and OP26; on the other hand, in a post-frontal situation there is not only cold advection, as observed in OP24 and OP27. To complete the analysis, Table 3 shows the synoptic situation for each campaign according to *Acevedo et al.* [2010] and also for each sub-region, with the average temperature advection determined by the model.

During OP23 only TF and BC sub-regions were sampled. TF region presents positive advection of 2.7 $^{o}$C/day while BC region has cold air advection with values of -0.8 $^{o}$C/day (Table 3). According to the classification of *Acevedo et al.* [2010], OP23 is a day 0 situation, characterized by weak frontal system over the BMC region; with the present mesoscale model results, this situation presented small negative (cold) temperature advection by westerly winds over the largest temperature gradient region, and positive (warm) temperature advection over the remaining domain, associated with northerly winds (Figure 4a).

The OP24 measurements covered the three sub-regions of BMC. Warm air temperature advection was observed over MC with values of 0.4 $^{o}$C/day, while both TF and BC sub-regions presented cold advection, with values of -3.2 and -11.6 $^{o}$C/day, respectively (Table 3). Very different from OP23, *Acevedo et al.* [2010] classified OP24 as day +2 as the frontal system had already crossed the BMC region, and a typical post-frontal condition is seen (Figure 4b). One can also note that the air temperature at 2 m approximately follows the SST distribution, and there is also a negative air temperature advection associated with southerly winds in the northern part of the BMC region, and positive temperature advection related to easterly winds over the southern BMC region.

The three mentioned sub-regions were sampled during OP25 campaign. Positive temperature advection of 7.8 and 8.5 $^{o}$C/day was observed over MC and TF, respectively, while BC sub-region presented negative advection of -4 $^{o}$C/day (Table 3). The OP25 situation is classified as day -2, meaning two days before the frontal passage, typically as a pre-frontal situation, with an anti-cyclonic dominance located east of the BMC region and positive air temperature advection associated with winds coming from the north (Figure 4c). Once again, air temperature at 2m follows SST distribution, and the corresponding thermal advection pattern presents negative

values south of the BMC also related to northerly winds; there is also a negative cold advection area located east-northeast of the BMC, related to the southeasterly component of the wind.

The OP26 radiosondes covered only the TF sub-region, where cold temperature advection of -15.3 $^{o}$C/day was observed. OP26 is a day -1 condition (Figure 4d), with the high-pressure center displaced east-northeast from the BMC region, yielding a northwest wind over almost all the modeled area. The air temperature at 2 m again follows the SST pattern, associated with negative temperature advection over the BMC region itself and positive values in the neighborhood.

OP27 measurements provided samples for the three sub-regions of BMC, which presented cold temperature advection of -6.8, -1.4 and -5.3 $^{o}$C/day, respectively (Table 3). The OP27 was classified as day+1 situation, a post-frontal condition associated with anti-cyclonic gyre close the BMC region, which is responsible for negative thermal advection over the whole area, except in the north of the BMC, where positive values are found.

These results show that the ocean thermal front has a strong signature on the air temperature at 2 m, and, due to its almost meridional orientation, temperature advection is strongly influenced by the zonal component of the wind. Another important aspect is the relative orientation of the atmospheric frontal system with the thermal ocean front, which makes it difficult to isolate the effects.

## 3.3 Vertical Structure of the MABL

The vertical MABL analysis was based on BRAMS results and considered average vertical sections crossing the thermal ocean front obtained with the GRD10/OBS setup. These averages in time were performed on those dates with the

radiosonde observations mentioned before, and they considered potential temperature and wind components up to 1200 meters high (Figure 5).

The average vertical section for OP23 shows intense vertical potential temperature gradient on the cold side of the front close to the surface, while the warm side presents weaker gradient (Figure 5a). In terms of the wind speed vertical section, one can note stronger winds over BC associated with weak vertical shear at the MABL from the surface up to approximately 250 meters high.

OP24 has a colder average potential temperature section compared to OP23, and almost no vertical gradient up to 700 meters high on both sides of the front. This homogeneity is also observed in wind speed, with almost no shear up to 500 m; stronger winds occurred at the warm side of the thermal ocean front (Figure 5b). OP25 presents an intense vertical gradient of potential temperature at the cold side, while the warm side shows no vertical gradient up to 700 m. The vertical shear is high on the cold side and almost non-existent over warmer waters (Figure 5c).

Once again, intense vertical potential temperature gradients and strong vertical shear are observed over cold waters in OP26 when compared with those values obtained on the warm side (Figure 5d). In terms of the vertical structure of the potential temperature and wind speed, the situation is similar for OP27 with more intense gradient at the cold side; on the other hand, the winds are stronger at the cold side, mainly in the region close to the thermal front (Figure 5e).

## 3.4 Stability and Momentum Budget Analysis

Very interesting aspects arose when comparing the mesoscale model results obtained with GRD10/OBS and GRD10/CLIM experiments. In this section we made the analysis of MABL conditions based on (i) comparisons between surface results from different model setups (GRD10/OBS versus GRD10/CLIM), (ii) the stability

parameter SST-SAT and used in the previous works of *Tokinaga et al.* [2005], *Pezzi et al.* [2005, 2009] and (iii) momentum equations terms. We tried to reveal and understand the predominance of some of the mentioned physical mechanisms in the air-sea interaction processes.

Besides the *in situ* radiosonde information, the most important difference between these experiments is that the SST specification varies from daily AMSR-E in GRD10/OBS to long-term monthly mean values in GRD10/CLIM. We computed the 24-hour average difference fields of SST, sea level pressure and surface winds (OBS-CLIM). Besides, to verify if the two mechanisms occur over the BMC region, we obtained the wind stress curl and divergence as well as the Laplacian of sea level pressure of these difference fields, according to *O'Neill et al.* [2010a].

When looking for the presence of stability changes mechanism, we superimposed fields of SST difference on wind curl for each campaign (Figure 6), and we could found correspondence between cyclonic curvatures over warmer waters during OP23, OP24 and OP27 (Figures 6a, 6b and 6e), as well as anticyclonic curvatures over cold water during OP25 (Figure 6c). This pattern is not absolutely clear with 24-hour average fields, but some correspondences were observed and could support the existence of the Wallace mechanism. On the other hand, OP25 and OP26 presented cyclonic patterns mainly on the interface (Figures 6c, 6d), as OP24 also did (Figure 6b).

For evaluating hydrostatic balance mechanism, we considered wind divergence and the laplacian of surface pressure for each set of observational data (Figure 7). In a general way, the model was able to capture the enhanced convergence (divergence) over warmer (colder) waters, with evident signatures occurring during OP25 and OP27 (Figures 7c and 7e) and less intense and evident for the other campaigns but

again with clear correspondence between the analyzed fields (Figures 7a, 7b and 7d). It's important to stress that these patterns are not absolutely clear, but they suggest the existence of the Lindzen & Nigam mechanism.

These findings make evident that both mechanisms can occur, even simultaneously. Their intensities vary significantly, making possible some predominance, depending obviously on the SST gradient and on the intensity of the synoptic system. Within this context, we decided to investigate through momentum budget equations how the mesoscale model represents these processes, and if it's possible to quantify them in a comparative way.

The SST difference between OBS and CLIM experiments superimposed on the corresponding surface pressure and wind difference reveals that, during OP23, stronger winds and lower atmospheric pressure values are located over warmer waters (Figure 8, upper panels). Comparing the magnitude of the pressure gradient terms in OBS and CLIM simulations for OP23, we found major differences at the interface for the zonal component and a confuse pattern for the meridional component over warm waters (Figure 8, middle and lower, left panels). Horizontal advection terms also changed when comparing OBS and CLIM experiments, but the magnitude of these changes are less relevant than the pressure gradient, and their differences are more detectable over the warm side (Figure 8, middle and lower, central panels). Fluctuation/residual terms also have their maximum differences at the interface (Figure 8, middle and lower, right panels). These findings, in a certain way, do not suggest predominance of Lindzen & Nigam or Wallace mechanisms. On the other hand, the flow shows a cross-front component from cold to warm side with increasing velocities and turning to the left, as explained by *O'Neill et al.* [2010b].

OP24 also presents stronger winds over relatively warmer waters, and the difference in surface pressure presents a more complex spatial structure (Figure 9, upper panels). Pressure gradient relevance is very clear over the whole area in this case (Figure 9, middle and lower, left panels), more prominent in the zonal direction, which is consistent with the observed stronger meridional winds over the warm side. In this case, advection terms seem to have secondary and restricted importance while fluctuation due to turbulence and friction appeared with relevant values but not directly related to stronger surface winds (Figure 9, middle and lower, right panels). Based on that, pressure gradient and turbulence influences were acting together to modify surface wind intensity. The flow has a cross-front component from cold to warm, increasing intensity and turning to the left, which again agrees very well with O'Neill *et al*. [2010b].

When comparing both model setups for OP25, one can note that the difference in surface pressure is always positive as well as an evident local minimum exactly over warm waters. The wind differences clearly show stronger changes over the front, but this time acting to decrease wind velocities in the cold side (Figure 10, upper panels). Both zonal and meridional pressure gradient terms have a clear signature due to the relative low located over the warm side of the front (Figure 10, middle and lower, left panels). Momentum advections show no evidences of its importance, but fluctuation due to turbulence and friction presents significant values, comparable in intensity to pressure gradient (Figure 10, middle and lower, right panels). This situation suggests coexistence of pressure gradient and turbulence, but now to decrease wind magnitude over the thermal front. The wind component normal to the front is evident from warm to cold side, with a decrease in velocities and a turn to the left, which

agree with *O'Neill et al.* [2010b] in terms of magnitude but not in direction of deflection.

OP26 comparisons for OBS and CLIM setup show lower values of surface pressure difference over warm waters in correspondence with changes in surface winds (Figure 11, upper panels). This situation is quite similar to OP23 in terms of synoptic conditions, structure of SST anomalies and modulation of the adjacent MABL, but this is not exactly the same for momentum budget terms. There are indications of zonal pressure gradient changes related to warmer waters (Figure 11, middle left panels), but the meridional component do not present this behavior (Figure 11, lower left panels). Momentum advection influence appears slightly related to cold water, but with small magnitude for both components (Figure 11, middle and lower, central panels). Residual terms representing turbulence and friction present their maximum change at some part of the thermal front for both components, but only the zonal component appears to be correlated to warmer waters (Figure 11, middle and lower, right panels). The cross-front wind from cold to warm is accelerated and turns to the left, again in agreement with *O'Neill et al.* [2010b].

OP27 experiments also show lower values of surface pressure for the OBS setup, once again with a local minimum over warm waters, a similar configuration compared to OP25. The wind differences show larger modifications over the thermal ocean front (Figure 12, upper panels), turning the wind without changing its intensity. The terms of momentum budget show large modifications at the most intense SST gradient region. For the three plotted terms, large values are found at the warm side of the front, with a clear contribution of advection and turbulence/friction terms to the wind modification due to the presence of the local minimum atmospheric pressure

(Figure 12, middle and lower panels). The wind blows a little bit transverse to the thermal front, crossing from warm to cold side at the northern part of the modeled area, where a turn to the right is observed without velocity change, which is in agreement with *O'Neill et al.* [2010b].

In a general way, the momentum budget terms add few specific evidences to clarify the eventual dominance of modulation mechanisms. In almost all the cases, vertical advection relevance was negligible in our experiments, except for OP23/2004 and OP27/2008 mainly over cold waters. Additionally, due to the pressure field difference between OBS and CLIM experiments, the most marked changes are almost always more relevant in pressure gradient and in fluctuation than in Coriolis and in advection terms. It's important to stress that this fact should not be always identified as the existence of both mechanisms.

Other relevant issue from these momentum budget analyses is related to the cross-front component. Results for OP23 and OP26 showed wind speed increase and turn to the left when the flow cross the thermal front from the cold to the warm side, which agree with the idea proposed by *Spall* (2007) and *O'Neill et al.* [2010b]. In any case, the relative orientation of the synoptic system to the thermal front is also a limiting factor, as well as the model performance at each situation.

Another point to be highlighted is the use of 24-hour averages for these determinations, which is inadequate for investigating high-frequency processes.

## 4. Concluding Remarks

This work discussed and analyzed five numerical atmospheric simulations assimilating observed data over the Western South Atlantic. The data were collected during five consecutive years from 2004 to 2008 (OP23 to OP27) as part of the

INTERCONF program in the BMC region. This work extends and complements previous studies of *Pezzi et al.* [2005, 2009] and *Acevedo et al.* [2010] where only observed data, collected by INTERCONF, were analyzed. To our knowledge, this is the first numerical atmospheric approach with *in situ* data assimilation conducted in the Brazil-Malvinas Confluence region to study air-sea interaction physical processes focusing on MABL stability. As remarked by *Pezzi et al.* [2009], despite the fact that this region is acknowledged as one of the most energetic regions of the world's oceans, very few studies have addressed the importance of studying its air-sea coupling processes.

We found evidence that the mechanism of modulation of surface winds in the region of the ocean front is greatly influenced by the SST pattern. Temperature advection patterns are characterized by interaction between the synoptic and the local scales; besides, there is a strong influence of the zonal wind component into the air temperature advection due to the ocean thermal front orientation, and also due to the relative orientation of the atmospheric frontal system.

The use of the BRAMS model to evaluate the presence and eventual dominance of wind modulation mechanisms was, in part, successful. Good correlation coefficients and low mean square errors supported the idea to use these results to further verification. The vertical sections of model results with AMSR-E and radiosonde data assimilation showed the impact of a permanent ocean thermal front over the lower adjacent atmosphere in different synoptic conditions, adding knowledge to those vertical sections based only on observed profiles.

Comparisons between OBS and CLIM model setups through simple subtraction between them could reveal some interesting aspects. When the SST-differences are superimposed to the wind-differences curl, there are evidences that support the static stability mechanism proposed by *Wallace et al.* [1989]. On the other hand,

considering wind divergence and the laplacian of surface pressure, we found another set of evidences about the hydrostatic balance mechanism proposed by *Lindzen & Nigam* [1987].

The analysis of momentum budget terms did not show a clear and reasonable explanation of the existence or predominance of the modulation mechanisms. More than this: it also revealed the relevance of other effects, such the idea proposed by *Spall* [2007], based on unbalanced Coriolis force, and also turbulence/friction effects obtained as the residual term of the momentum budget equations.

Thus it is not surprising that modulation mechanisms co-exist, with or without predominance in the MABL instability processes. Despite the fact that this has been observed in our experiments using 24-hour average fields, it was not part of the scope of this study to give more importance to one or to the other in the process analyzed. At this stage of development, we could not generalize beyond one or other mechanism or any predominance. The reason for that might be related by shortness of our observed time series and, consequently, short numerical experiments.

The confluence of BC and MC generates high thermal contrast with high spatial and time variability, and this contrast is also observed in the adjacent atmosphere. The pattern of surface temperature advection in the BMC region is largely influenced by the ocean front meandering position, whose combination with the advection caused by the local circulation pattern produces different temperatures when compared to the study conducted by *Acevedo et al.* [2010]. The pattern of the BMC temperature advection can locally change the thermodynamic pattern, consequently influencing the vertical transport of momentum on both sides of the front ocean.

This study was mainly focused on the description of physical mechanisms and the understanding of the air-sea interactions that occur at the BMC region. Previous studies, such as *Tokinaga et al.* [2005], *Pezzi et al.* [2005, 2009], and *Acevedo et al.*

[2010] were not conclusive in terms of the impacts of SST in the hydrostatic balance on the MABL following *Lindzen and Nigam* [1987] hypothesis. The probable reason for this is the lack of sufficient resolution data or lack of spatial coverage. This was not the case in the present study, where high horizontal resolution numerical experiments were conducted, in which observed radiosonde data were assimilated into the simulations and, finally, the results were analyzed and compared to observations.

## Acknowledgments

## References

ACEVEDO, O.C.; PEZZI, L.P.; SOUZA, R.B.; ANABOR, V.; DEGRAZIA, G. Atmospheric boundary layer adjustment to the synoptic cycle at the Brazil-Malvinas Confluence, South Atlantic Ocean. *J. Geophys. Res.*, v. 115, p. D22107, 2010.

BARNES, S.L. A technique for maximizing details in numerical weather map analysis. *J. Appl. Meteorol.*, 3(4), 396–409, 1964.

CHELTON, D.B.; XIE, S.-P. Coupled ocean-atmosphere interaction at oceanic mesoscales. *Oceanography,* 23(4):52–69, 2010.

COTTON, W.R.; PIELKE, R.A.; WALKO, R.L.; LISTON, G.E.; TREMBACK, C.J.; JIANG, H.; MCANELLY, R.L.; HARRINGTON, J.Y.; NICHOLLS, M.E.; CARRIO, G.G.; MCFADDEN, J.P. RAMS 2001: Current status and future directions. *Meteorology and Atmospheric Physics*, 82, n. 1–4, 5–29, 2003.

HOFFMAN, R.N.; LEIDNER, S.M. An Introduction to the Near-Real-Time QuikScat Data. *Wea. Forecasting*, 20, 476–493, 2005.

KALNAY, E., and Coauthors The NCEP/NCAR 40-Year Reanalysis Project. *Bull. Amer. Meteor. Soc.*, 77, 437–471, 1996.

LEGECKIS, R. Long waves in the eastern equatorial Pacific Ocean: A view from a geostationary satellite, *Science*, 197, 1179–1181, 1977.

LENTINI, C.A.D.; CAMPOS, E.J.D.; OLSON, D.B.; PODESTÁ, G.P. Sea Surface Temperature Anomalies in the Western South Atlantic from 1982 to 1994. *Cont. Shelf Res.*, v. 21, n.1, p. 89–112, 2001.

LENTINI, C.A.D.; GONI, G.J.; OLSON, D.B. Investigation of Brazil Current rings: 1993-1998. *J. Geophys. Res.*, EUA, v. 111, p. 1–17, 2006.

LINDZEN, R.S; NIGAM, S. On the role of Sea Surface Temperature gradients in forcing low-level winds and convergence in the tropics. *J. Atmos. Sci.*, 44(17), 2418–2436, 1987.

LIU, W.; XIE, X.; POLITO, P.S.; XIE, S,-P.; HASHIZUME, H. Atmospheric Manifestation of Tropical Instability Wave Observed by QuickSCAT and Tropical Rain Measuring Mission. *Geophys. Res. Lett.*, 27(16), 2545–2548, 2000.

OLSON, D.B.; PODESTÁ, G.P.; EVANS, R.H.; BROWN, O.B. Temporal variations in the separation of Brazil and Malvinas Currents. *Deep-Sea Res.*, 35, 1971–1990, 1988.

O'NEILL, L.W.; CHELTON, D. B.; ESBENSEN, S. K. The Effects of SST-Induced Surface Wind Speed and Direction Gradients on Midlatitude Surface Vorticity and Divergence. *J. Clim.*, 23, 255–281, 2010a.

O'NEILL, L.W.; ESBENSEN, S. K.; THUM, N.; SAMELSON, R. M.; CHELTON, D. B. Dynamical analysis of the boundary layer and surface wind responses to mesoscale SST perturbations. *J. Clim.*, 23, 559–581, 2010b.

PEZZI, L.P.; VIALARD, J.; RICHARDS, K.J.; MENKES, C.; ANDERSON, D. Influence of ocean-atmosphere coupling on the properties of Tropical Instability Waves. *Geophys. Res. Lett.*, 31, n.L16306, p. L16306, 2004.

PEZZI, L.P.; SOUZA, R.B.; DOURADO, M.S.; GARCIA, C.A.E.; MATA, M.M.; SILVA-DIAS, M.A.F. Ocean-Atmosphere in Situ Observations at the Brazil-Malvinas Confluence Region. *Geophys. Res. Lett.*, 32, L22603, 2005.

PEZZI, L.P.; SOUZA, R. B.; ACEVEDO, O.; WAINER, I.E.K.; MATA, M.M.; GARCIA, C.A.E.; CAMARGO, R. Multi-year measurements of the Oceanic and Atmospheric Boundary Layers at the Brazil-Malvinas Confluence Region. *J. Geophys. Res.*, v. 114, p. 1–10, 2009.

PIELKE, R.A.; COTTON, W.R.; WALKO, L.R.; TREMBACK, C.J.; LYONS, W.A.; GRASSO, L.D.; NICHOLLS, M.E.; MORAN, M.D.; WESLEY, D.A.; LEE, T.J.; COPELAND, J.H. A comprehensive meteorological modeling system – RAMS. *Meteorology and Atmospheric Physics*, 49, 69–91, 1992.

PODESTÁ, G.P. Utilización de datos satelitarios en investigaciones oceanográficas y pesqueras en El Océano Atlántico Sudoccidental, In E.E. Boschi (Ed.), *El mar argentino y sus recursos pesqueros*, Tomo 1 (pp. 195–222). Mar del Plata, Argentina: Instituto Nacional de Investigación y Desarrollo Pesquero (INIDEP), 1997.

REID, J.L.; NOWLIN JR., W. D.; PATZERD, W.C. On the characteristics and circulation of the Southwestern Atlantic Ocean. *J. Phys. Oceanogr.*, 7, 62–91, 1977.

SEO, H.; MILLER, A.J; ROADS, J.O. The Scripps Coupled Ocean–Atmosphere Regional (SCOAR) Model, with Applications in the Eastern Pacific Sector. *J. Clim.*, 20, 381–402, 2007a.

SEO, H.; JOCHUM, M.; MURTUGUDDE, R.; MILLER, A.J.; ROADS, J.O. Feedback of Tropical Instability-Wave-Induced Atmospheric Variability onto the Ocean. *J. Clim.*, 20, 5842–5855, 2007b.

SMALL, R.J.; XIE, S.-P.; WANG, Y.; ESBENSEN, S.K.; VICKERS, D. Numerical simulation of boundary layer structure and crossequatorial flow in the eastern Pacific. *J. Atmos. Sci.*, 62, 1812–1830, 2005.

SMALL, R.J.; DESZOEKE, S.P.; XIE, S.P.; O'NEILL, L.; SEO, H.; SONG, Q.; CORNILLON, P.; SPALL, M.; MINOBE, S. Air–sea interaction over ocean fronts and eddies. *Dynamics of Atmospheres and Oceans*, 45, 274–319, 2008.

SOUZA, R. B.; MATA, M.M.; GARCIA, C.A.E.; KAMPEL, M.; OLIVEIRA, E.N.; LORENZZETTI, J.A. Multi-sensor satellite and in situ measurements of a warm core ocean eddy south of the Brazil-Malvinas Confluence region. *Remote Sensing of Environment*, EUA, v. 100, p. 52–66, 2006.

SOUZA, R.B.; ROBINSON, I.S. Lagrangian and satellite observations of the Brazilian Coastal Current. *Cont. Shelf Res.*, 24, 241–262, 2004.
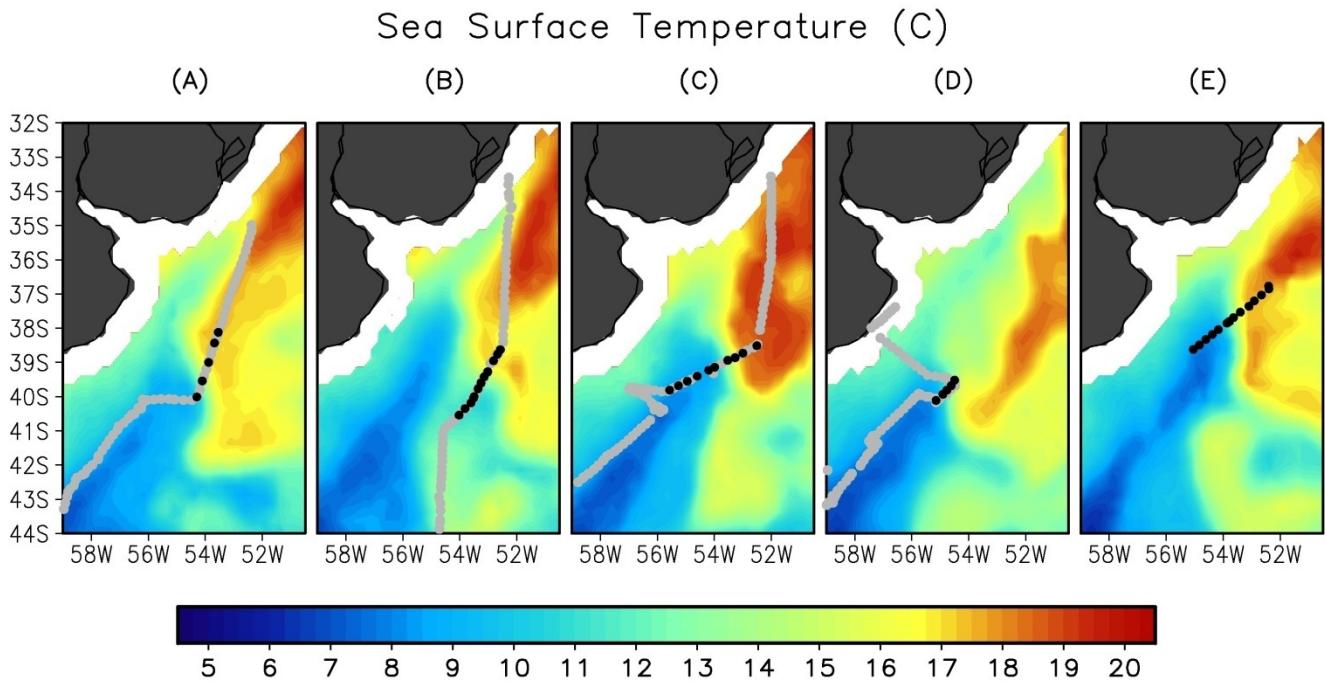
SPALL, M. A. Midlatitude Wind Stress–Sea Surface Temperature Coupling in the Vicinity of Oceanic Fronts. *J.Clim.*, 20(15), 3785–3801, 2007.

TOKINAGA, H.; TANIMOTO, Y.; XIE, S.-P. SST-induced surface wind variations over the Brazil-Malvinas Confluence: Satellite and in situ observations. *J. Clim.*, 18, 3470–3482, 2005.
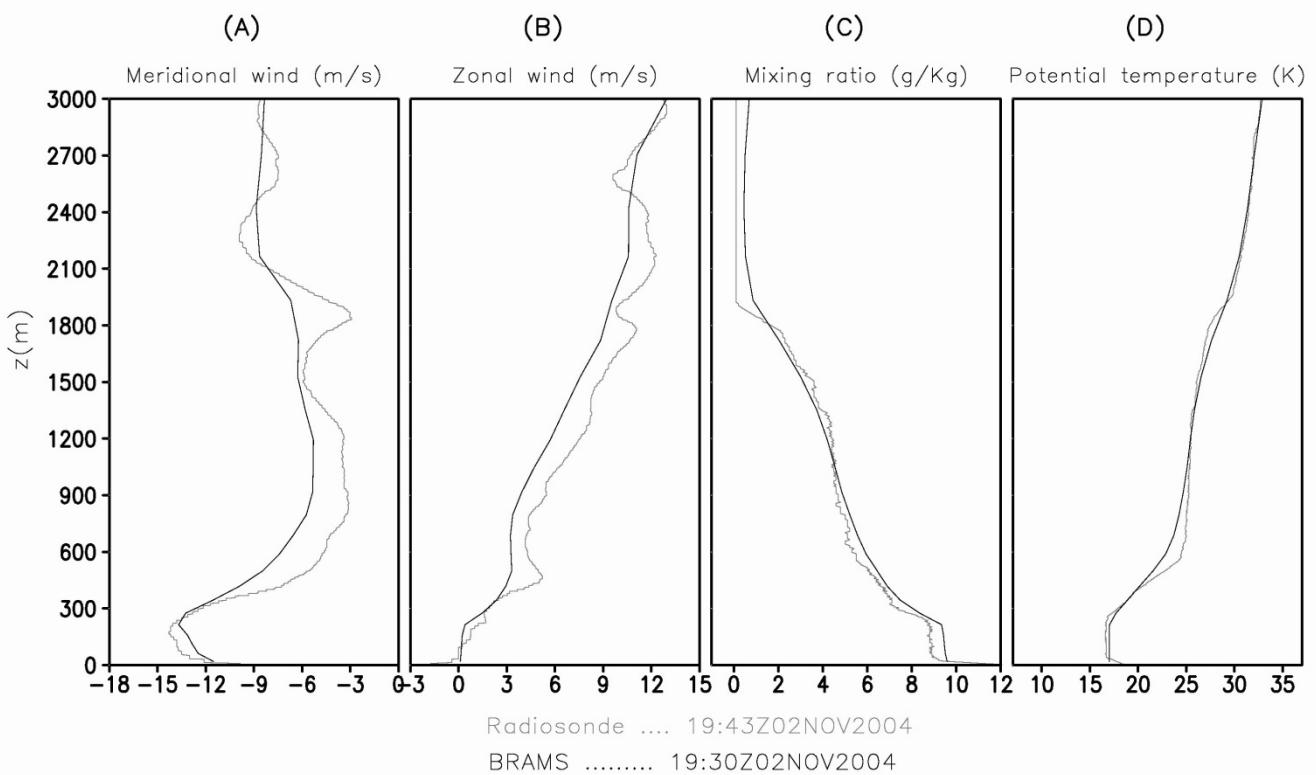
WALLACE, J.M.; MITCHELL, T. P.; DESER, C.J. The Influence of Sea-Surface Temperature on Surface Wind in the Eastern Equatorial Pacific:Weekly to Monthly Variability. *J. Clim.*, 2, 1492–1499, 1989.

WENTZ, F.J.; SMITH, D.K.; MEARS, C.A.; GENTEMANN, C.L. Advanced algorithms for QuikScat and SeaWinds/AMSR, IEEE 2001 International Geoscience and Remote Sensing Symposium, IGARSS '01, vol.3, pp. 1079–1081, 2001. doi: 10.1109/IGARSS.2001.976752

# Sea Surface Temperature (C)
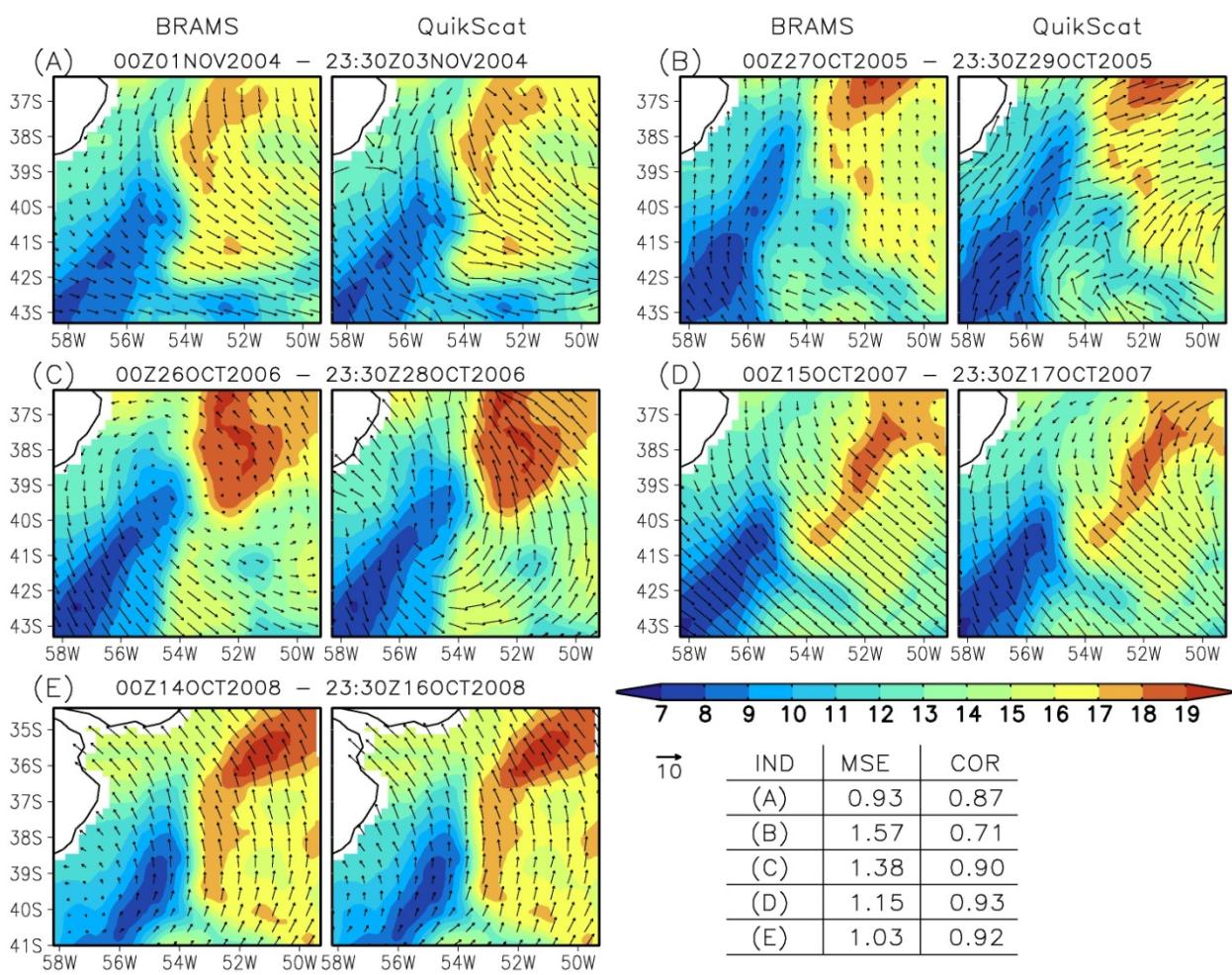


**Figure 1.** SST maps obtained by AMSR-E sensor of the Acqua Satellite at the BMC region. The dots represent the route of the *OSS Ary Rongel*. The grey dots are related to the surface data of ship's meteorological station, and the black dots are radiosondes and XBT positions. Panel A: November 2004, OP23; Panel B: October 2005, OP24; Panel C: October 2006, OP25; Panel D: October 2007, OP26; and Panel E: October 2008, OP27.

**Figure 2.** Vertical profiles at 38.12°S 53.55°W for 2nd November 2004, OP23. Black lines are the model results at 19:30Z; grey lines are observations at 19:43Z. Panel A: meridional wind; Panel B: zonal wind; Panel C: mixing ratio; and Panel D: potential temperature.
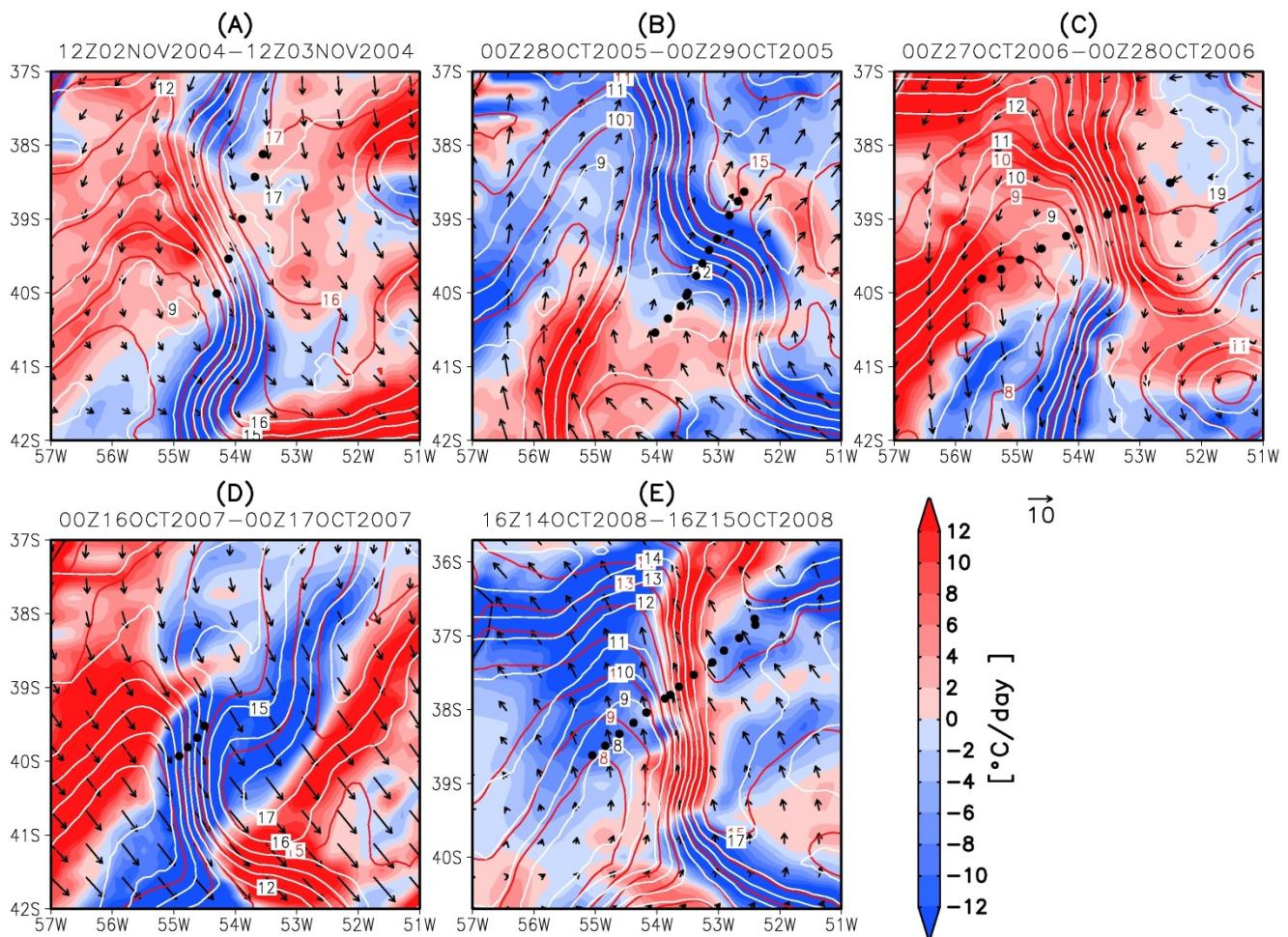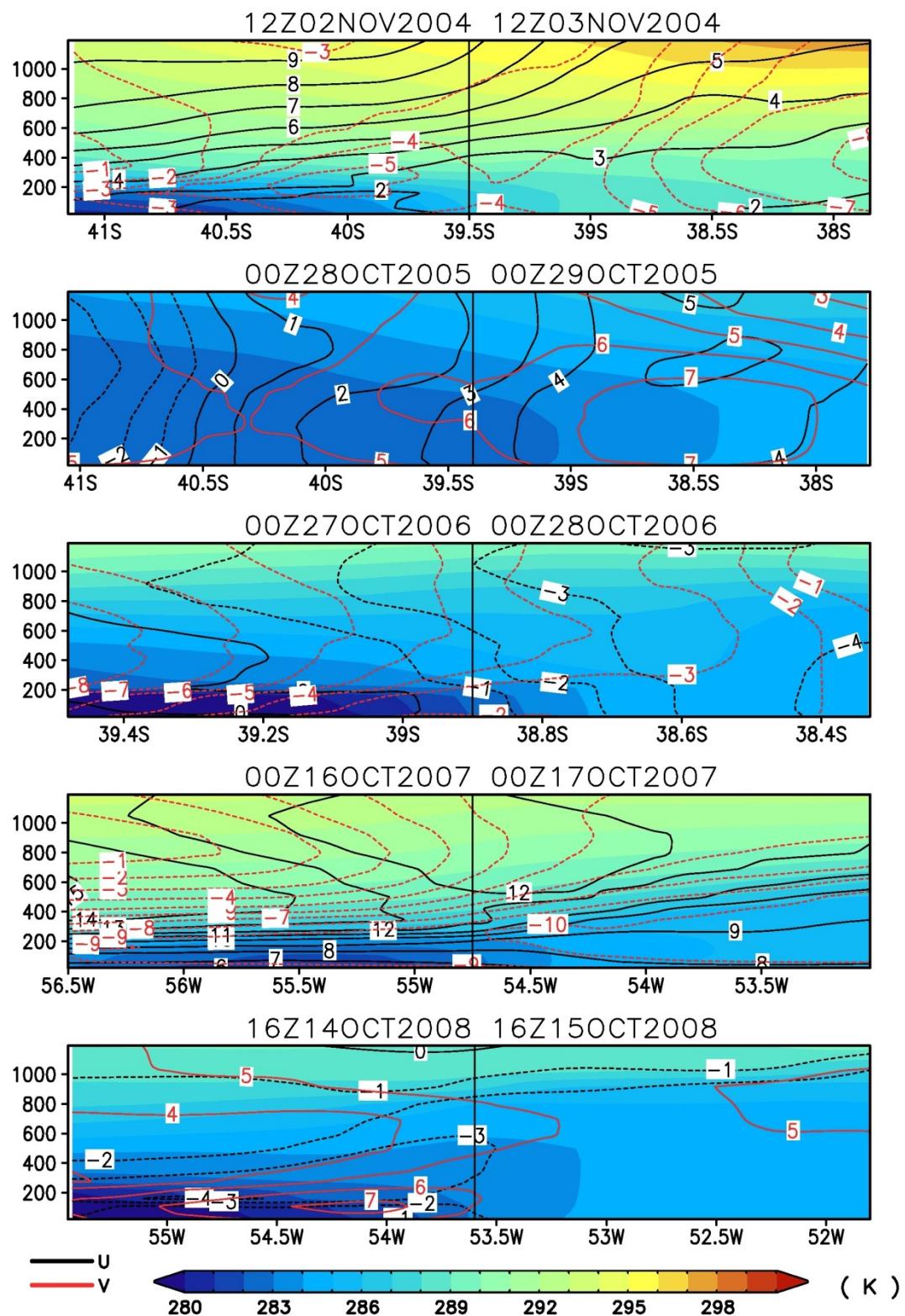
**Figure 3.** 3-day average fields of 10 m height winds (vectors, in m/s) of GRD10/OBS modeled results (left) and QuikScat observations (right) superposed on SST observed distribution (colorbar, in $^{o}$C). The values of mean square error (MSE) and correlation coefficient (COR) are shown lower right. Panel A: 1st November 2004 to 3rd November 2004, OP23; Panel B: 27th October 2005 to 29th October 2005, OP24; Panel C: 26th October 2006 to 28th October 2006, OP25, Panel D: 15th October 2007 to 17th October 2007, OP26; and Panel E: 14th October 2008 to 16th October 2008, OP27.
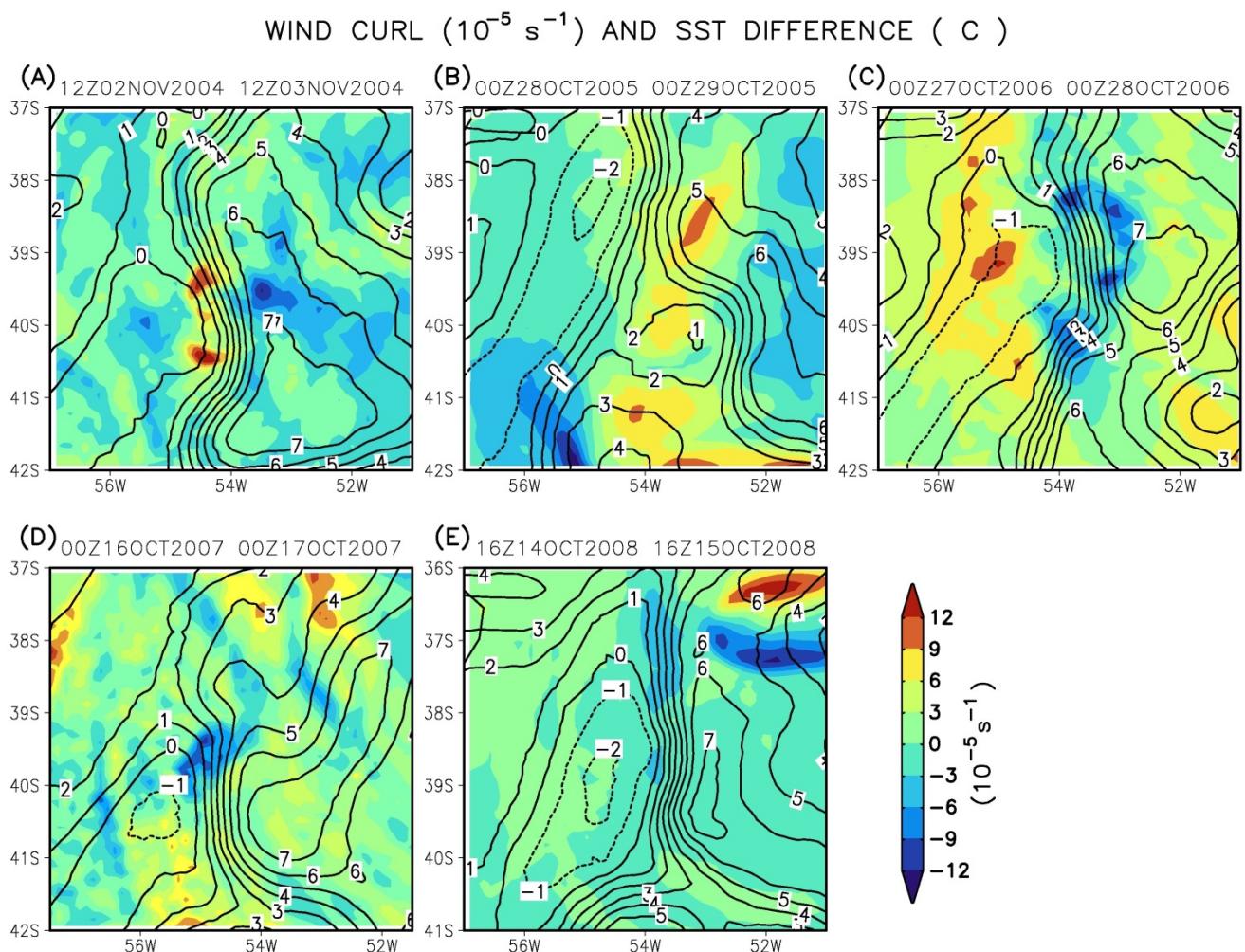
## Surface Temperature Advection



**Figure 4.** 24-hour average fields centered on the radiosonde (black dots) measurements date for each campaign, according to GRD10/OBS experiments. The 10 m high wind vectors (vectors, in m/s), SST (white contours, in °C), air temperature at 2m high (red contours, in °C) and surface thermal advection (color scale, in °C/day). Panel A: OP23; Panel B: OP24; Panel C: OP25; Panel D: OP26; and Panel E: OP27.
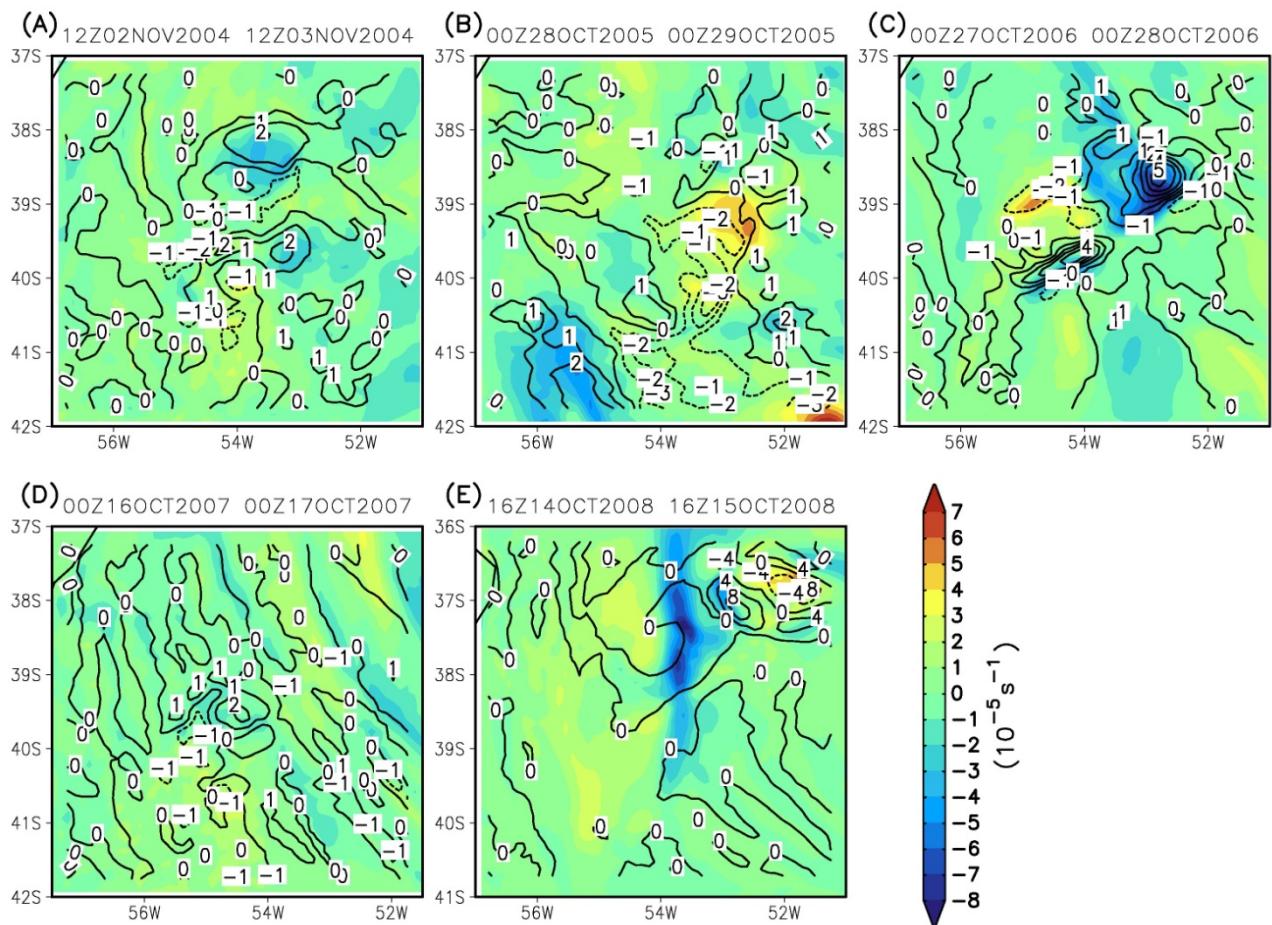
**Figure 5**. 24-hour average vertical sections of GRD10/OBS model results: potential temperature (colorbar, K), zonal wind component (black contours, in m/s) and meridional wind component (red contours, in m/s). From top to bottom: November 2004, OP23; October 2005, OP24; October 2006, OP25; October 2007, OP26 and October 2008, OP27.

WIND CURL ($10^{-5}$ s$^{-1}$) AND SST DIFFERENCE ( C )
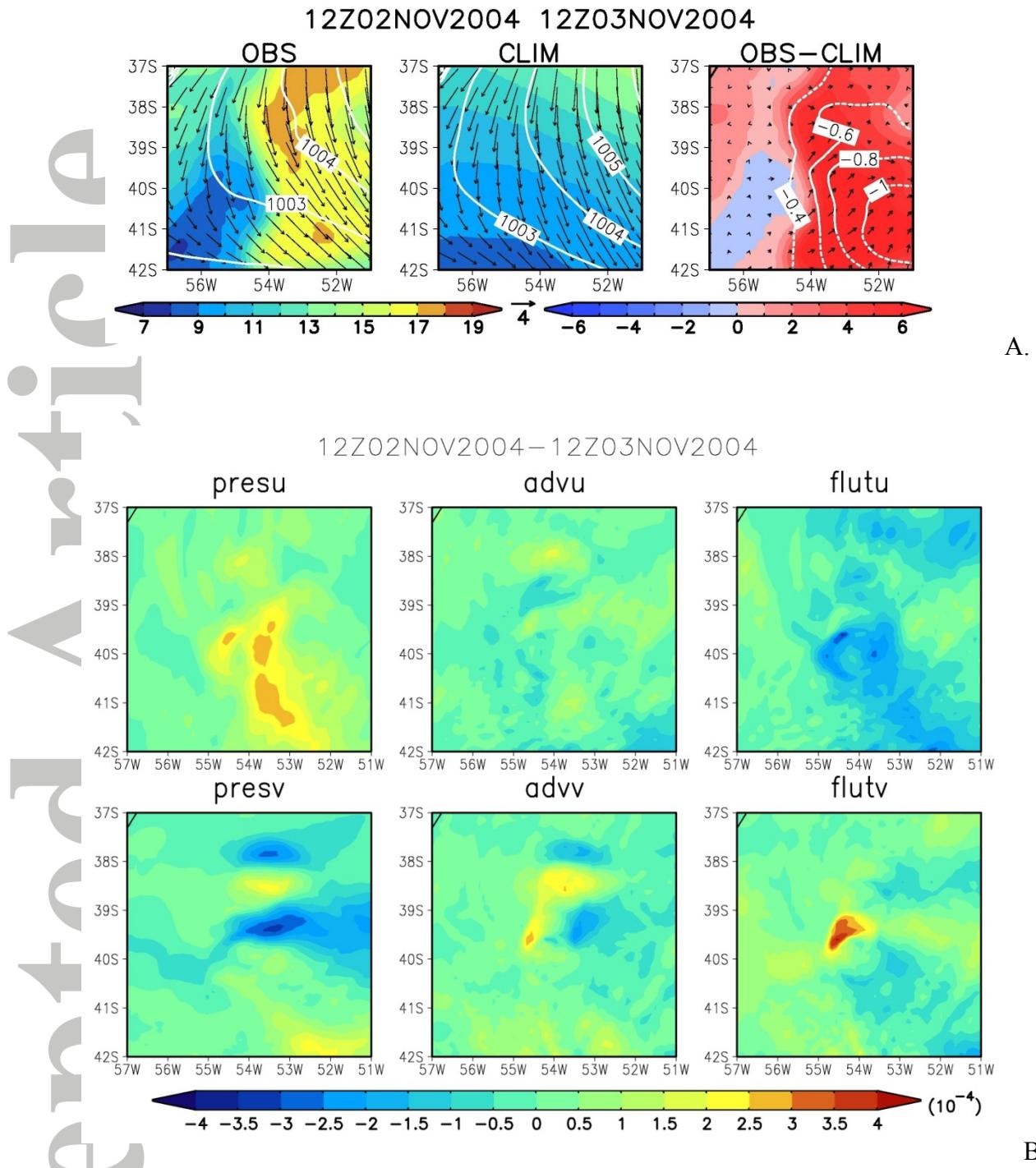
**Figure 6**. 24-hour average difference fields OBS-CLIM centered on the radiosondes measurements date for each campaign. Surface delta-wind curl (color, in $10^{-5}$s$^{-1}$) and delta-sst (contours, in °C). Panel A: OP23; Panel B: OP24; Panel C: OP25; Panel D: OP26; and Panel E: OP27.

WIND DIVERGENCE ($10^{-5}$ s$^{-1}$) AND LAPLACIAN OF PRESSURE ($10^{-10}$hPa.m$^{-2}$)
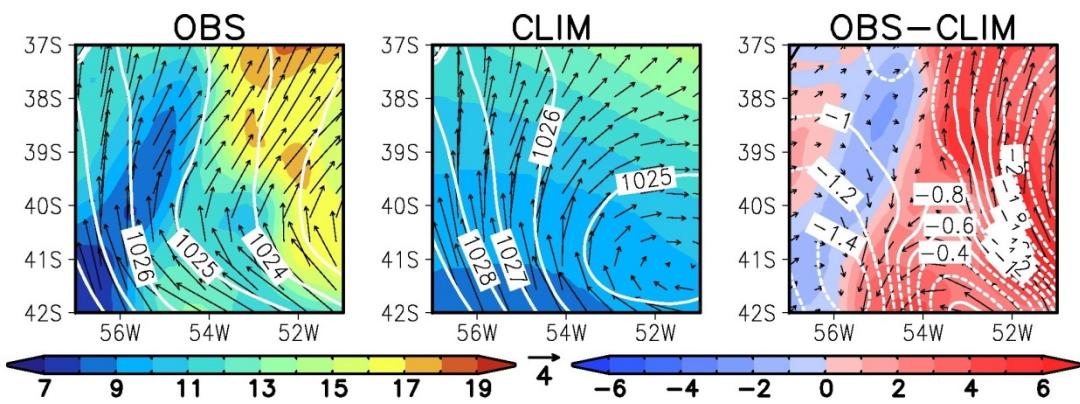
**Figure 7**. 24-hour average difference fields OBS-CLIM centered on the radiosondes measurements date for each campaign. Surface delta-wind divergence (color, in $10^{-5}$s$^{-1}$) and laplacian of surface delta-pressure (contours, in $10^{-10}$ hPa.m$^{-2}$). Panel A: OP23; Panel B: OP24; Panel C: OP25; Panel D: OP26; and Panel E: OP27.
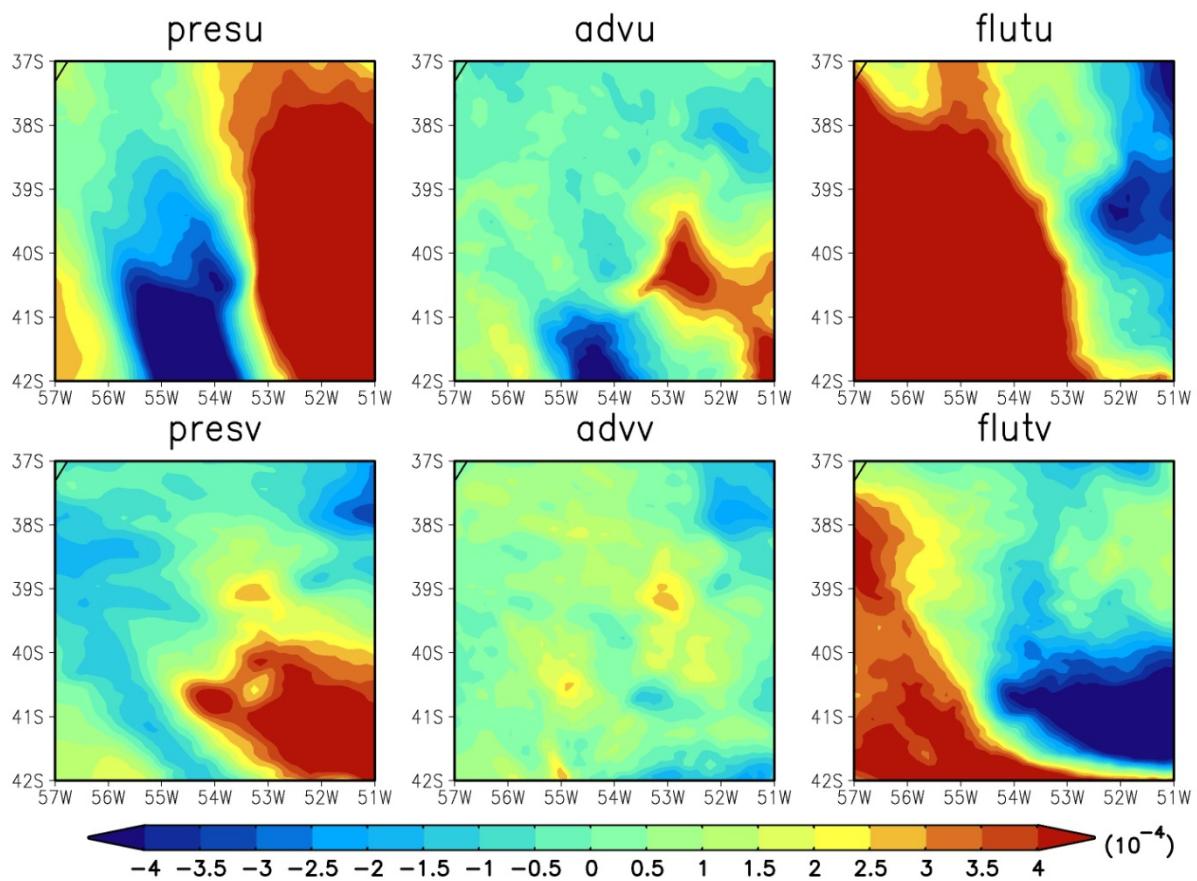
**Figure 8**. 24-hour averages of GRD10 model results for OP23. Upper: surface winds (black arrows, in m/s), SST (color, in °C) and sea level pressure (white contours, in mb) for the OBS simulations (left column), CLIM (central) and the difference fields OBS-CLIM (right column). Middle and lower: horizontal distribution of the difference fields OBS-CLIM related to the zonal (middle panels) and meridional (lower panels) momentum budget terms (in $10^{-4}$ m.s$^{-2}$) of pressure gradient (left column), advection (horizontal + vertical, central column) and fluctuation (right column).

## 00Z28OCT2005 00Z29OCT2005



A.
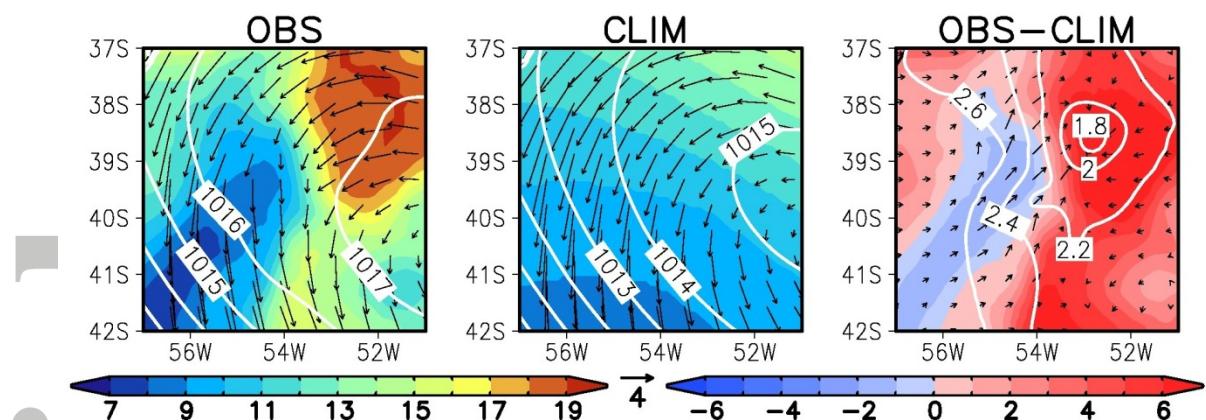
## 00Z28OCT2005-00Z29OCT2005



B.
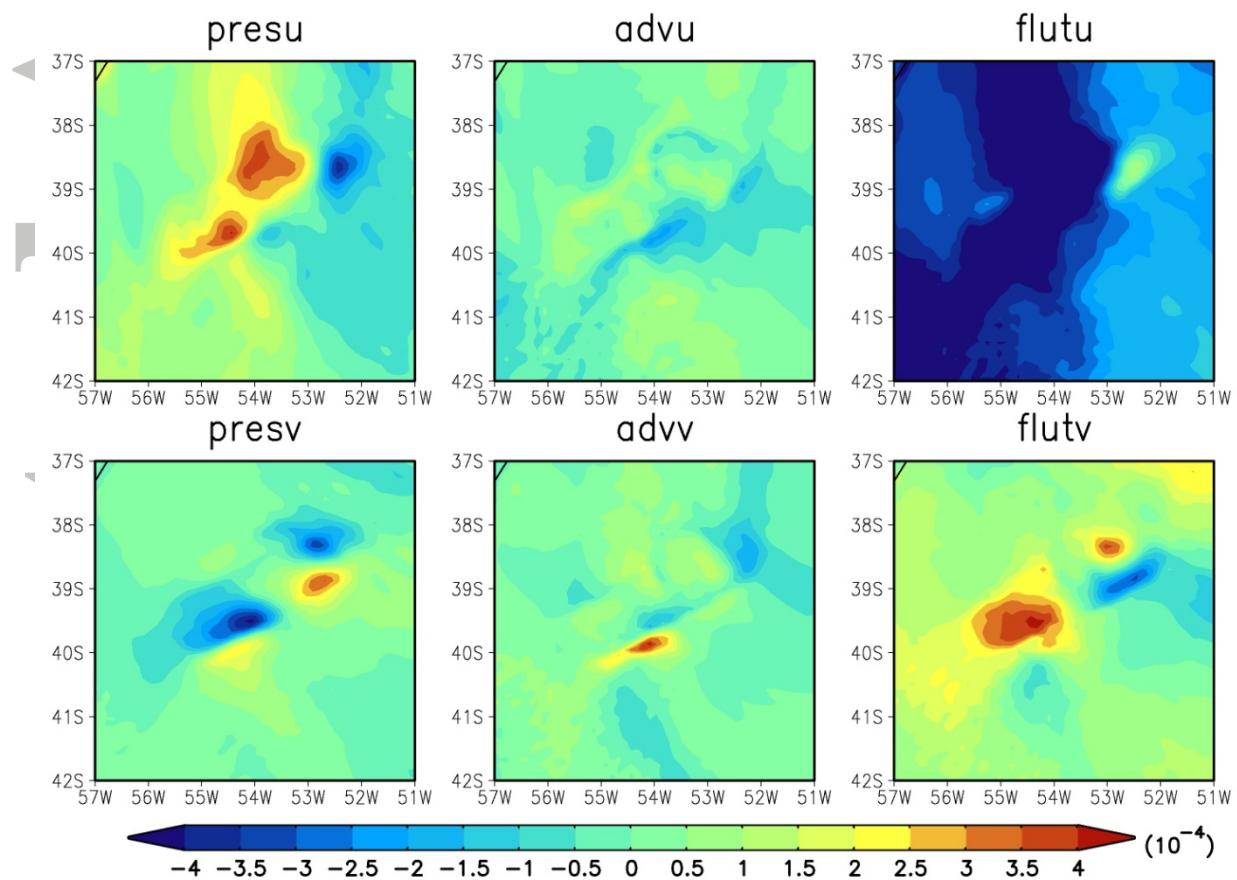
**Figure 9**. Same as Figure 8, but for OP24.

00Z27OCT2006  00Z28OCT2006

OBS    CLIM    OBS−CLIM



00Z27OCT2006−00Z28OCT2006

presu    advu    flutu

presv    advv    flutv

$(10^{-4})$
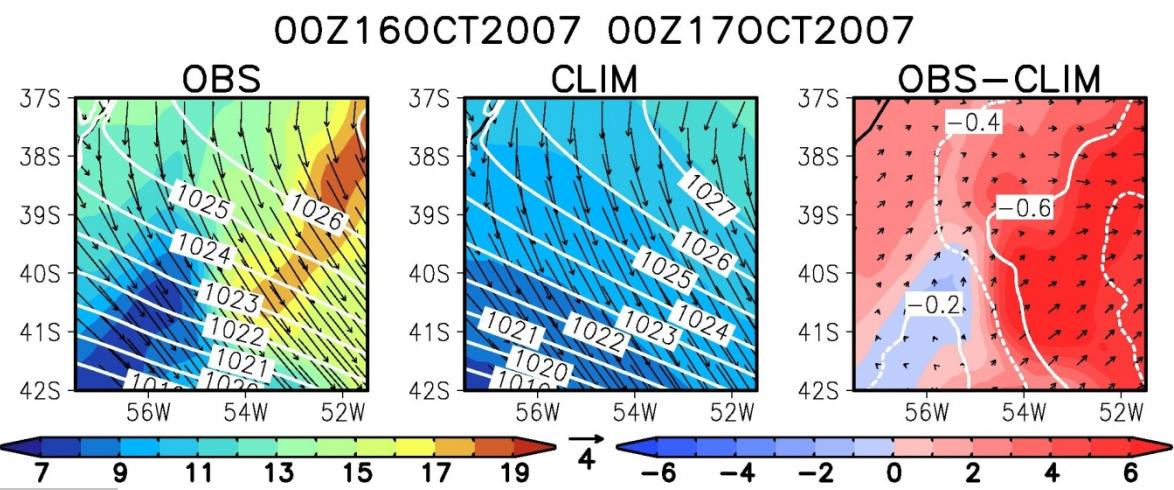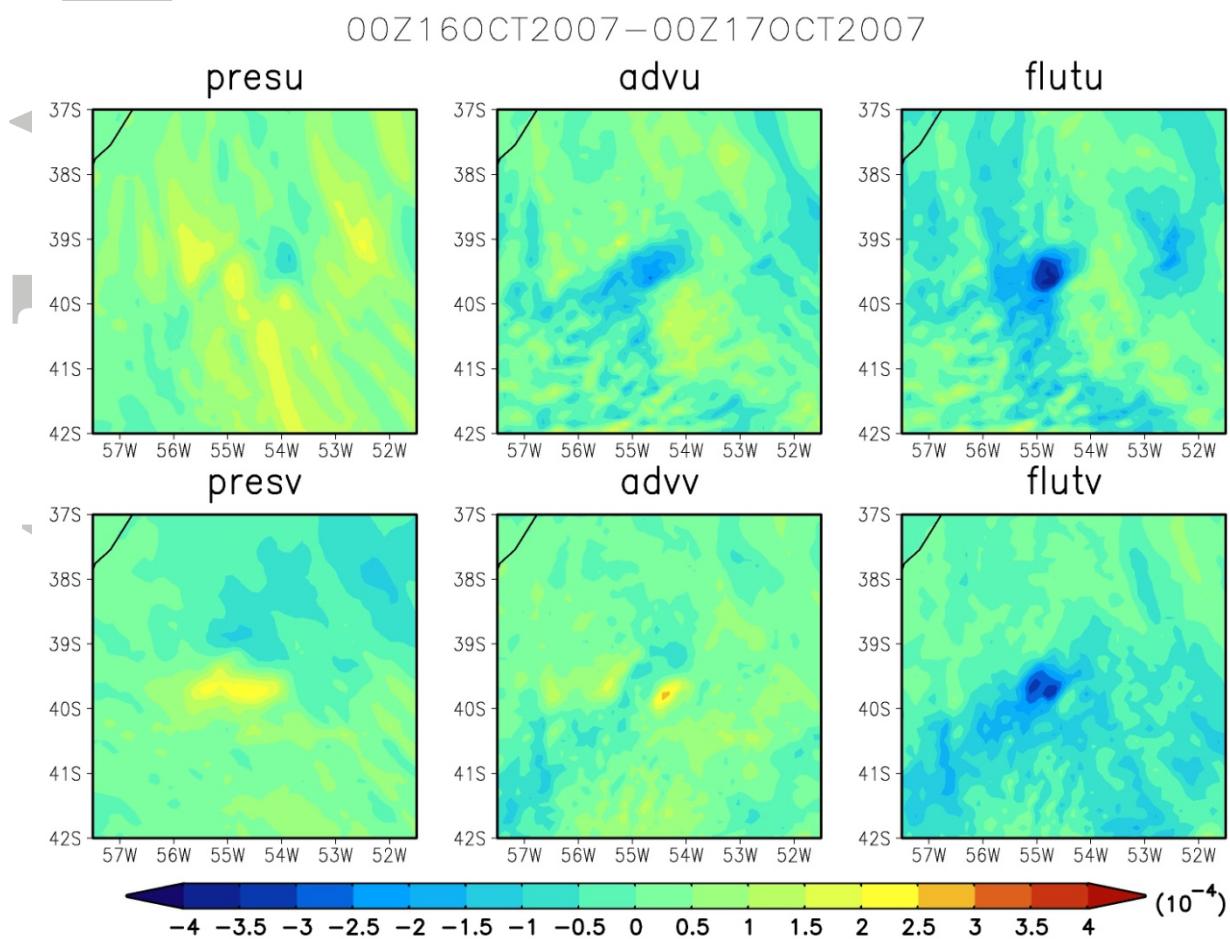
**Figure 10**. Same as Figure 8, but for OP25.
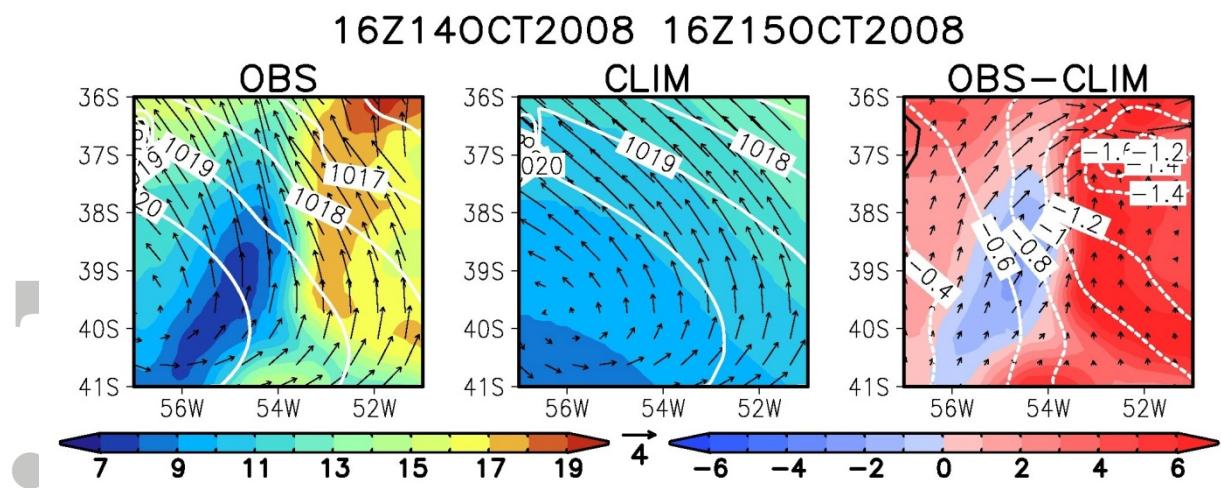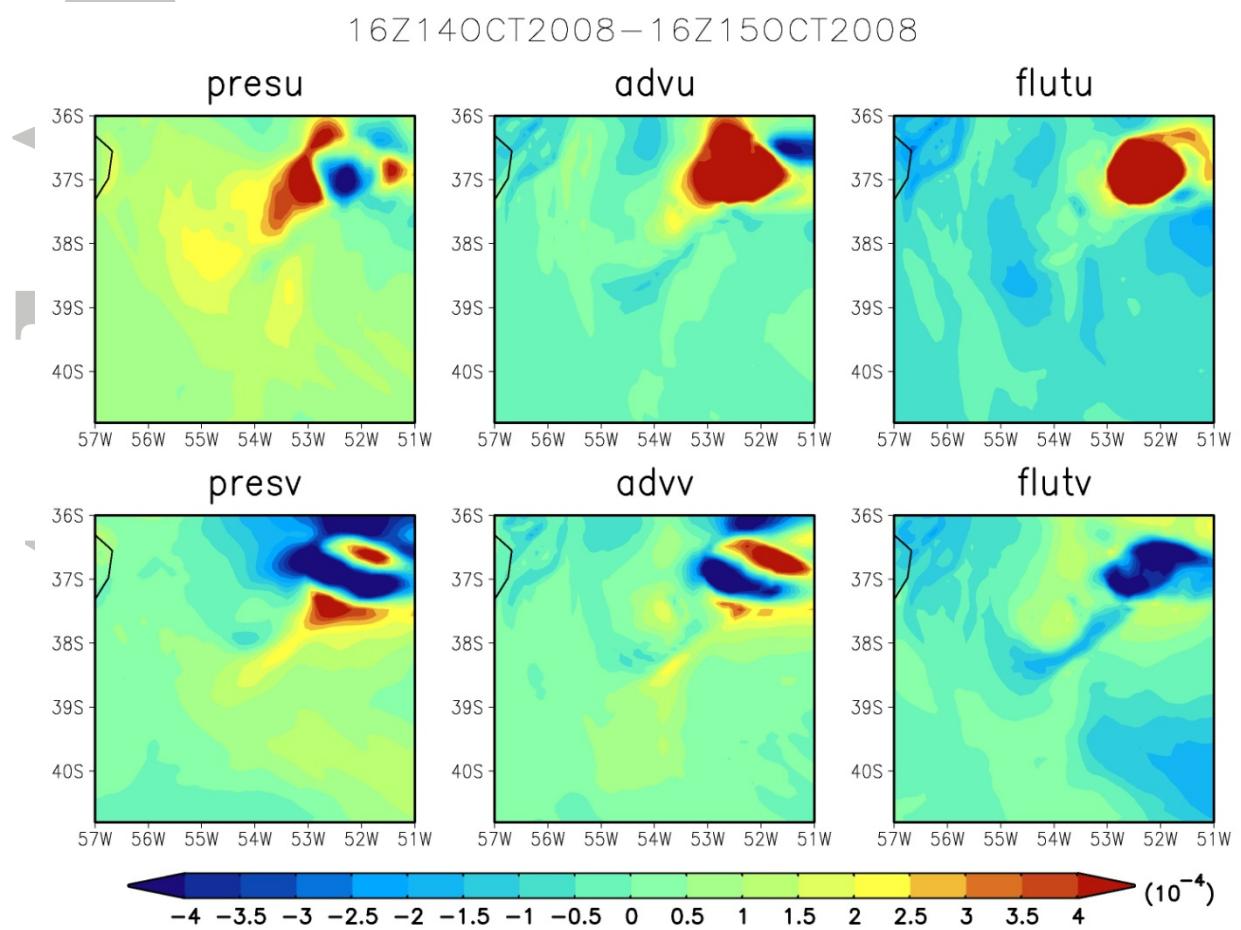
**Figure 11**. Same as Figure 8, but for OP26.

## 16Z14OCT2008  16Z15OCT2008



A.

## 16Z14OCT2008−16Z15OCT2008



B.

**Figure 12**. Same as Figure 8, but for OP27.

**Table 1**. Antarctic operation (OP), date, time of the measurement, position of the launch of radiosondes and position. Brazilian Current (BC), Thermal Front (TF) and Malvinas Current (MC).

| Exp | Date | time(UTC) | Lat(S) | Lon(W) | Side |
|---|---|---|---|---|---|
| **OP23** | 2 November 2004 | 1943 | 38.12 | 53.55 | BC |
| | 2 November 2004 | 2130 | 38.43 | 53.68 | BC |
| | 3 November 2004 | 0022 | 39.00 | 53.89 | BC |
| | 3 November 2004 | 0200 | 39.54 | 54.11 | TF |
| | 3 November 2004 | 0518 | 40.01 | 54.30 | TF |
| **OP24** | 28 October 2005 | 0232 | 38.63 | 52.58 | BC |
| | 28 October 2005 | 0329 | 38.76 | 52.68 | BC |
| | 28 October 2005 | 0451 | 38.95 | 52.82 | BC |
| | 28 October 2005 | 0714 | 39.27 | 53.02 | TF |
| | 28 October 2005 | 0811 | 39.42 | 53.15 | TF |
| | 28 October 2005 | 0916 | 39.60 | 53.26 | TF |
| | 28 October 2005 | 1024 | 39.77 | 53.36 | TF |
| | 28 October 2005 | 1201 | 40.00 | 53.50 | MC |
| | 28 October 2005 | 1322 | 40.04 | 53.52 | MC |
| | 28 October 2005 | 1421 | 40.18 | 53.61 | MC |
| | 28 October 2005 | 1619 | 40.35 | 53.82 | MC |
| | 28 October 2005 | 1746 | 40.54 | 54.03 | MC |
| **OP25** | 27 October 2006 | 1251 | 38.51 | 53.51 | BC |
| | 27 October 2006 | 1351 | 38.73 | 53.00 | TF |
| | 27 October 2006 | 1502 | 38.86 | 53.27 | TF |
| | 27 October 2006 | 1615 | 38.94 | 53.53 | TF |
| | 27 October 2006 | 1812 | 39.14 | 53.99 | TF |
| | 27 October 2006 | 1913 | 39.23 | 54.20 | MC |
| | 27 October 2006 | 2104 | 39.40 | 54.60 | MC |
| | 27 October 2006 | 2247 | 39.55 | 54.95 | MC |
| | 28 October 2006 | 0022 | 39.68 | 55.26 | MC |
| | 28 October 2006 | 0153 | 39.81 | 55.57 | MC |
| **OP26** | 16 October 2007 | 0512 | 39.52 | 54.50 | TF |
| | 16 October 2007 | 0706 | 39.68 | 54.62 | TF |
| | 16 October 2007 | 0806 | 39.81 | 54.77 | TF |
| | 16 October 2007 | 1000 | 39.93 | 54.91 | TF |
| **OP27** | 14 October 2008 | 1638 | 36.85 | 52.40 | BC |
| | 14 October 2008 | 1954 | 36.77 | 52.41 | BC |
| | 14 October 2008 | 2240 | 37.03 | 52.66 | BC |
| | 15 October 2008 | 0104 | 37.20 | 52.91 | BC |
| | 15 October 2008 | 0335 | 37.36 | 53.10 | TF |
| | 15 October 2008 | 0523 | 37.53 | 53.40 | TF |
| | 15 October 2008 | 0644 | 37.69 | 53.64 | TF |
| | 15 October 2008 | 0803 | 37.85 | 53.87 | TF |
| | 15 October 2008 | 1013 | 38.04 | 54.17 | TF |
| | 15 October 2008 | 1239 | 38.18 | 54.38 | MC |
| | 15 October 2008 | 1411 | 38.33 | 54.61 | MC |
| | 15 October 2008 | 1715 | 38.49 | 54.84 | MC |
| | 15 October 2008 | 1847 | 38.62 | 55.05 | MC |

**Table 2**. Experiment names, period descriptions, and associated days of the synoptic cycles (Source: *Acevedo et al.,* 2010).

| Experiment | Dates | Closest Frontal Passage Day | Condition | Estimated Thermal Advection ($^{o}$C day$^{-1}$) |
|---|---|---|---|---|
| OP23 | 2-3 November 2004 | 2 November 2004 | day 0 | -2.1 |
| OP24 | 28 October 2005 | 25 October 2005 | day +2 | -5.8 |
| OP25 | 27-28 October 2006 | 29 October 2006 | day -2 | 6.3 |
| OP26 | 16 October 2007 | 17 October 2007 | day -1 | 4.2 |
| OP27 | 14-15 October 2008 | 12 October 2008 | day +1 | -13.0 [a] |

[a]Cross frontal estimated thermal advection ($^{o}$C day$^{-1}$)

**Table 3**. Antarctic Operation name, day of the associated synoptic cycle and thermal advection determined by the model as function of the position. Malvinas Current (MC), Thermal Front (TF) and Brazilian Current (BC).

| Experiment | Synoptic Cycle | Thermal Advection (°C day$^{-1}$) | | |
|:---:|:---:|:---:|:---:|:---:|
| | | MC | TF | BC |
| OP23 | day 0 | ------- | 2.7 | -0.8 |
| OP24 | day +2 | 0.4 | -3.2 | -11.6 |
| OP25 | day -2 | 7.8 | 8.5 | -4.0 |
| OP26 | day -1 | ------- | -15.3 | ------- |
| OP27 | day +1 | -6.8 | -1.4 | -5.3 |